CHEMISTRY OF MATERIALS

pubs.acs.org/cm

Article

N-Heterocyclic Carbene Overlayers on Mild Steel

Lila Laundry-Mottiar, Thilini Malsha Suduwella, Waruni G. K. Senanayake, Matthew J. Turnbull, Antoine Juneau, Ekrupe Kaur, Mark D. Aloisio, Thiago M. Guimarães Selva, Jeffrey D. Henderson, Heng-Yong Nie, Mark Biesinger,* James J. Noel,* Yolanda S. Hedberg,* Cathleen M. Crudden,* and Janine Mauzeroll*

Cite This: *Chem. Mater.* 2025, 37, 76−86

Read Online

ACCESS | Metrics & More | Article Recommendations | Supporting Information

ABSTRACT: Although the functionalization of noble metals with N-heterocyclic carbenes (NHCs) is well-known, the interactions of these versatile ligands with common alloys are not. Herein, we present an immersion-deposition approach that enables the modification of mild steel (MiS) with diisopropylbenzimidazolium hydrogen carbonate (^{iPr}**NHC·H$_2$CO$_3$**). The NHC-modified surface was characterized by X-ray photoelectron spectroscopy, angle-resolved X-ray photoelectron spectroscopy, atomic force microscopy-based infrared spectroscopy, time-of-flight secondary ion mass spectrometry, and matrix-assisted laser desorption/ionization time-of-flight mass spectrometry. These experimental methods provide support for the functionalization of mild steel with ^{iPr}**NHC** and for the reduction of surface oxide by the carbene. Electrochemical analyses and salt immersion tests were also performed and they showed that the NHC coating increases the corrosion resistance of MiS. This study demonstrates that immersion deposition is a viable method for the modification of mild steel surfaces with N-heterocyclic carbenes and shows the potential for mitigating corrosion.

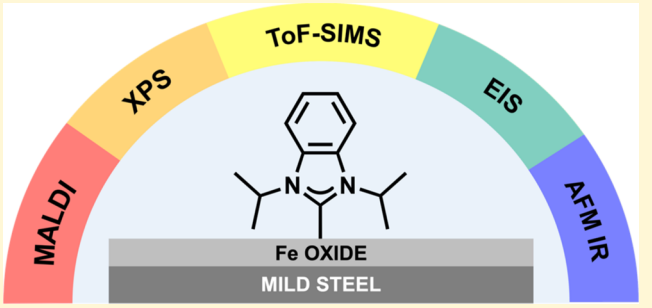

1. INTRODUCTION

Steel is a ubiquitous material, extensively used in construction and transportation due to its strength and durability.[1−3] Because of its widespread use, protecting steel from corrosion is a multibillion-dollar industry.[4,5] The majority of anticorrosion technologies employ coatings[6−11] that are physically adhered (i.e., physisorbed[12]) to metal surfaces. Over time, these coatings delaminate, resulting in corrosion and significant waste.[13−15]

Recently, N-heterocyclic carbenes (NHCs) have attracted interest for their ability to form stable films on a variety of metal surfaces.[16−31] In molecular chemistry, NHCs are known for their strong covalent bonds with transition metals,[32,33] which have translated into stable self-assembled monolayers on a variety of metal surfaces, including Au, Cu, Ag, Pt, Ru, Pd, and Co.[16,18,19,21,34−39]

Scanning tunneling microscopy has shown that NHCs form densely packed and highly ordered structures on metal surfaces, with surface orientation depending largely on the steric effects induced by the substituents on the two nitrogen atoms.[28,40−43]

Despite these promising studies, the use of NHCs in protecting the most globally employed alloy, steel, has never been reported. Compared to noble metals, steel has a more complex surface that is much more susceptible to corrosion.[44] Although steel has yet to be explored, the NHC-functionalization of an iron oxide surface by electrodeposition has recently been found to lead to interactions between the metal and NHC as well as the metal oxide and NHC.[45]

Herein, we describe methods to prepare and characterize ^{iPr}**NHC**-modified mild steel (MiS) surfaces, where ^{iPr}**NHC** = 1,3-bis(2,6-diisopropylphenyl)imidazol-2-ylidene. NHC-modified and unmodified MiS surfaces were examined by matrix-assisted laser desorption/ionization time-of-flight mass spectrometry (MALDI ToF-MS), time-of-flight secondary ion mass spectrometry (ToF-SIMS), X-ray photoelectron spectroscopy (XPS), angle-resolved XPS (ARXPS), atomic force microscopy-based infrared spectroscopy (AFM-IR), and scanning electron microscopy with energy dispersive X-ray spectroscopy (SEM−EDX). Using this multianalytical approach, oxide thickness changes were quantified, oxide compositional changes were identified, and the coverage of the ^{iPr}**NHC** layer on MiS was elucidated. Electrochemical impedance

Received: June 28, 2024
Revised: December 10, 2024
Accepted: December 11, 2024
Published: December 24, 2024

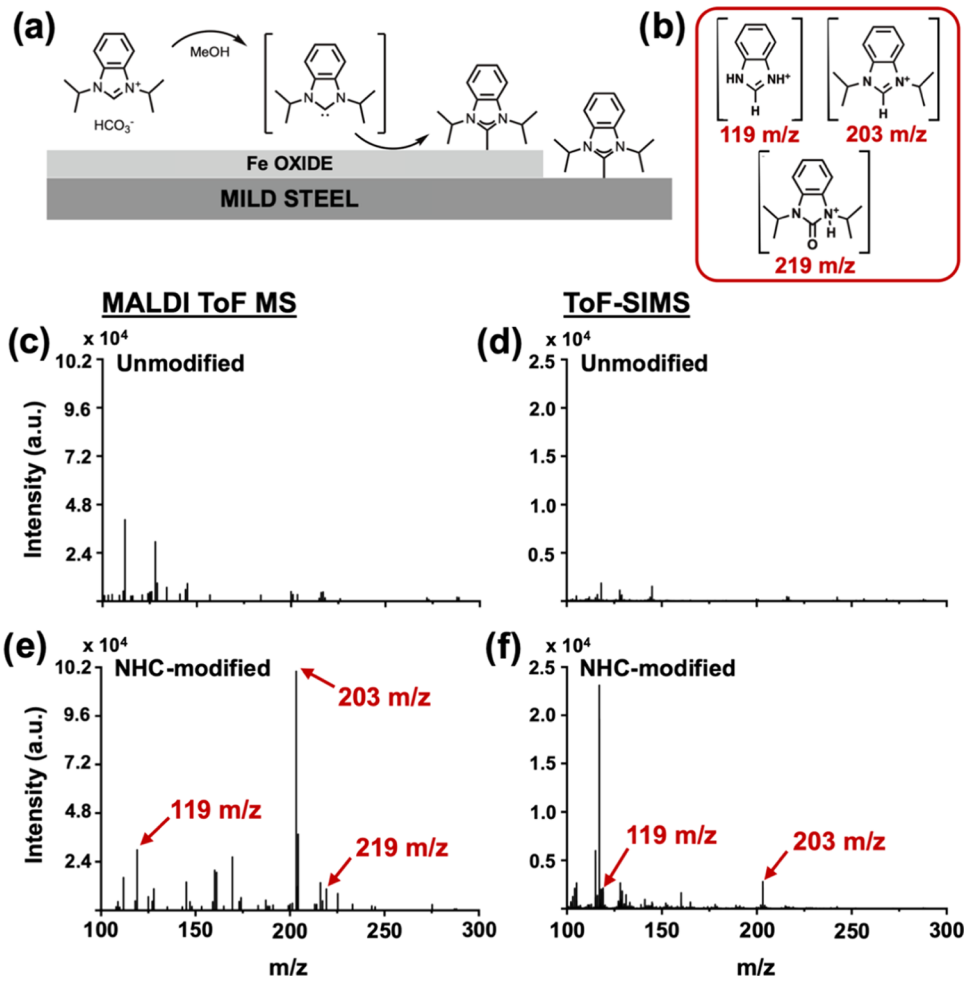

Figure 1. (a) Schematic demonstrating the immersion deposition of ^{iPr}**NHC** on mild steel. (b) Molecular structures of ^{iPr}**NHC**-related ions observed by mass spectrometry. Mass spectra of unmodified MiS were obtained by MALDI (c) and ToF-SIMS (d). Mass spectra of NHC-modified MiS by MALDI (e) and ToF-SIMS (f) with signals appearing at 119 m/z (fragment ion) and 203 m/z (pseudomolecular ion) indicating successful deposition. A signal at 219 m/z (NHC-urea ion) is also observed by MALDI (e), possibly indicating an iron oxide reduction process.

spectroscopy (EIS) and potentiodynamic polarization (PDP) measurements, along with a salt immersion test, were also carried out to determine the corrosion resistance of the NHC layer. These corrosion tests revealed an increase in corrosion resistance after NHC deposition both numerically (by fitting) and visually (by optical microscopy).

2. RESULTS AND DISCUSSION

2.1. Functionalizing Mild Steel with ^{iPr}NHC. ^{iPr}**NHC**·H_2CO_3 was employed as the NHC precursor based on its extensive use in the literature.[17,18,28,37,38,40,42,46,47] In this study, films of ^{iPr}**NHC** were also found to have superior thermal stability compared to counterparts with smaller substituents on nitrogen (ToF-SIMS spectra found in Figures S3 and S4). Prior to deposition, the MiS coupons were polished using P1200 SiC paper and cleaned by sonication in 2-propanol followed by acetone (see Supporting Information, Sections 1.1−1.4 for experimental methods). Immersion deposition was carried out for 24 ± 0.5 h at room temperature (RT) under quiescent conditions with 5 mM solutions of ^{iPr}**NHC**·H_2CO_3 in MeOH. After deposition, the coupons were rinsed four times with MeOH for 1 min each rinse.

Immersion deposition resulted in the functionalization of MiS by ^{iPr}**NHC** as determined by the observation of a signal at 203 m/z ($C_{13}N_2H_{19}^+$) in both MALDI and ToF-SIMS spectra (Figure 1e,1f), corresponding to the singly charged ^{iPr}**NHC**$^+$ pseudomolecular ion (full ToF-SIM spectra found in Figure S5). The term pseudomolecular ion is here used to denote that the NHC ion is protonated, and formed during the ionization process of the techniques. This ion was detectable even after the washing procedure, indicating an interaction with the surface that is stronger than simple adsorption. MALDI and ToF-SIMS (positive secondary ion mode) mass spectrometry also revealed a fragment signal at 119 m/z ($C_7N_2H_7^+$), validating the presence of ^{iPr}**NHC** on MiS (Figure 1e,1f). As further validation of the pseudomolecular ion's identity, the NHC + 1 isotope was observed at 204 m/z, which was only present at the correct natural abundance (C13% + N15%) for ToF-SIM spectra (see mass spectra in Figure S6). To increase the complexity of the surface, similar ToF-SIMS experiments were run on stainless steel (SS) 304 and high strength steel (HSS), which also show peaks at 203 and 119 m/z (ToF-SIM spectra found in Figures S7 and S8). A peak at 219 m/z ($C_{13}N_2H_{19}O^+$) was also observable by MALDI mass spectra (Figure 1e) and is attributed to NHC-urea (^{iPr}**NHC═O**). This peak has been observed in previous studies and was found to be caused by the reduction of copper oxide to copper metal.[21] Thus, the observation of this signal may be an

https://doi.org/10.1021/acs.chemmater.4c01804
Chem. Mater. 2025, 37, 76−86

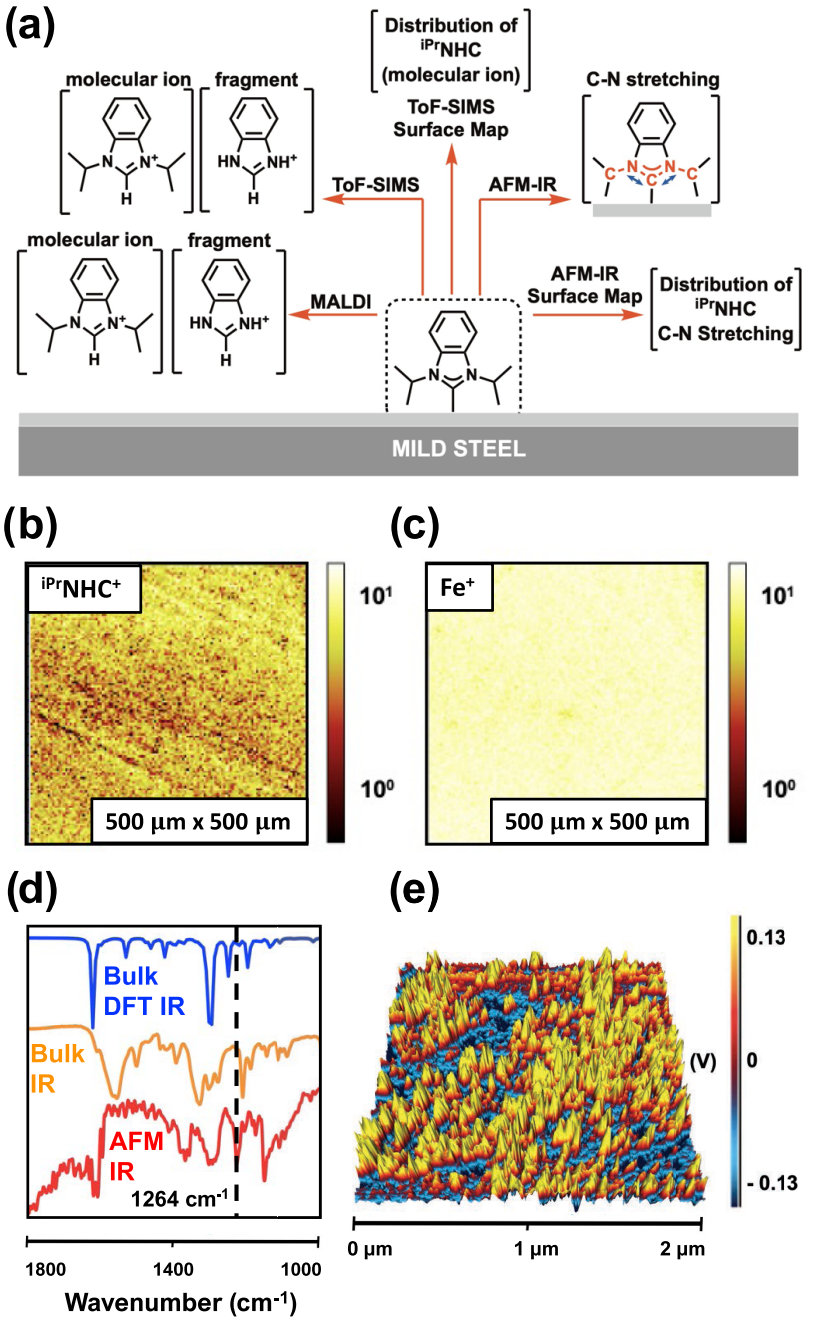

Figure 2. (a) Schematic demonstrating that the presence of the ^{iPr}**NHC** was confirmed on MiS by MALDI, ToF-SIMS, and AFM-IR. (b) ToF-SIMS surface map of the $C_{13}N_2H_{19}^+$ ion on NHC-modified MiS. (c) ToF-SIMS surface map of the Fe^+ ion on NHC-modified MiS. (d) DFT-calculated IR spectrum of bulk ^{iPr}**NHC·H$_2$CO$_3$** (blue), experimental Fourier transform infrared spectroscopy (FTIR) spectrum of bulk ^{iPr}**NHC·H$_2$CO$_3$** (orange), and experimental AFM-IR spectrum of NHC-modified MiS (red), highlighting the C−N stretching frequency at 1264 cm^{-1}. (e) AFM-IR surface map of NHC-modified MiS tuned to the C−N stretching frequency at 1264 cm^{-1} (yellow = highest density of C−N stretch).

indication of the involvement of NHC in the reduction of iron oxide.

Using density functional theory (DFT) at the B3LYP/def2-TZVP level within the SMD solvation model for acetonitrile (CH_3CN), we determined that the energy required for the formation of the reactive carbene from the ^{iPr}**NHC** precursor, via proton transfer to the HCO_3^- moiety, is ΔG = +79.9 kJ/mol (see Supporting Information, Section 1.17 for details). This process was calculated to be barrierless, indicating that it should readily occur at room temperature. This supports the feasibility of NHC deposition using simple immersion methods. DFT calculations also confirmed that the formation of ^{iPr}**NHC═O** is particularly thermodynamically favorable, with a free energy change of ΔG = −306 kJ/mol (if formed from 1/2 O_2). This suggests that ^{iPr}**NHC═O** is a likely byproduct when it is exposed to potential oxygen sources such as iron oxide, supporting its formation under our experimental conditions.

Thermogravimetric analysis (TGA) was attempted to monitor the degradation of the NHC deposit upon exposure to elevated temperature; however, these experiments were

https://doi.org/10.1021/acs.chemmater.4c01804
Chem. Mater. 2025, 37, 76−86

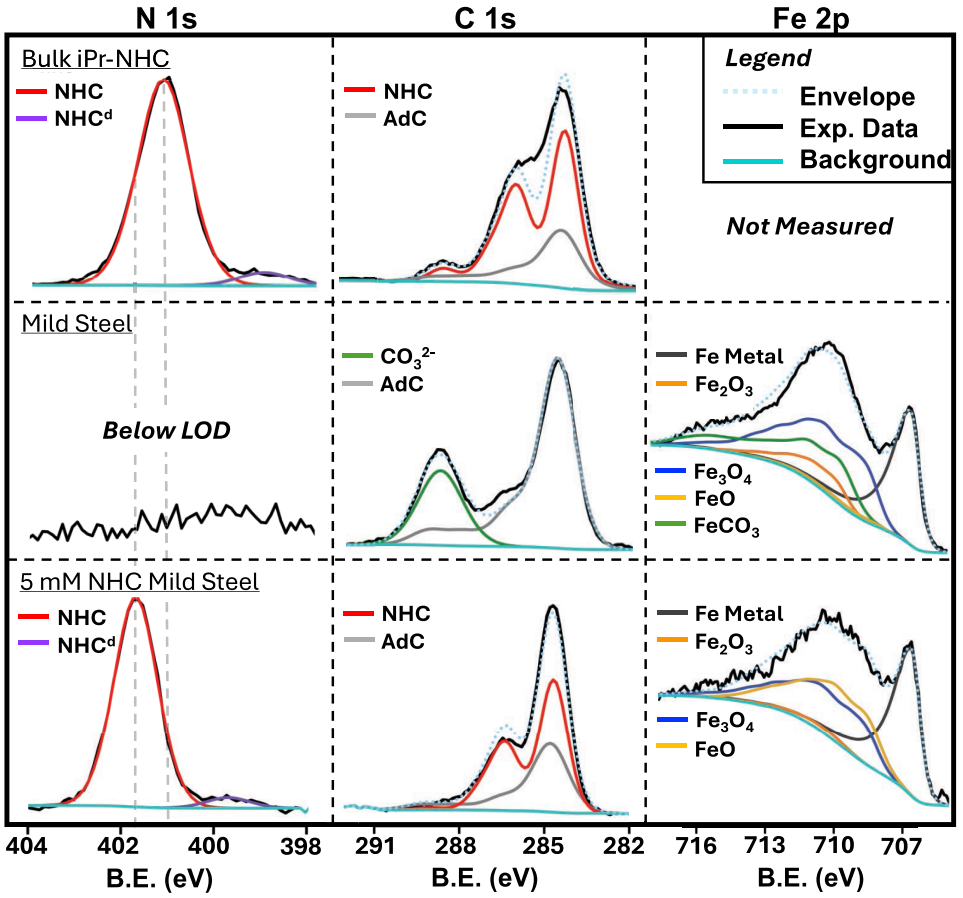

Figure 3. N 1s, C 1s, and Fe 2p high-resolution XP spectra of bulk ^{iPr}**NHC·H$_2$CO$_3$**, MiS that was immersed in MeOH for 24 h (control), and ^{iPr}**NHC**-modified MiS (AdC = adventitious carbon, NHC^d = NHC degradation product, LOD = limit of detection). Note: Fe 2p XP spectra were not collected for the bulk powder, as ^{iPr}**NHC·H$_2$CO$_3$** is not expected to contain any Fe.

unsuccessful because of the low mass of the NHC layer. The TGA data can be found in Figure S9.

2.2. Surface Distribution of ^{iPr}NHC on Modified Mild Steel. Having confirmed effective MiS surface functionalization with ^{iPr}**NHC**, we next interrogated the surface distribution by using ToF-SIMS and AFM-IR spectroscopic mapping. The ToF-SIMS map of the $C_{13}N_2H_{19}^+$ parent ion (Figure 2b) shows a wide coverage of ^{iPr}**NHC** over the MiS surface (detectable in 99.4% of pixels, details in Supporting Information, Section 1.11), confirming NHC-overlayer formation. ToF-SIMS analysis also revealed a slight attenuation of the Fe^+ ion (55.9 m/z) intensity after deposition (Figure S10), which supports the presence of a thin ^{iPr}**NHC** film since the probing depth of ToF-SIMS is 1−3 nm.[48] The (attenuated) Fe^+ ion signal was mapped across an ^{iPr}**NHC**-modified MiS coupon as shown in Figure 2c.

To provide more information about the NHC distribution on a smaller scale than that obtained with ToF-SIMS, we performed AFM-IR mapping (using a mirror-polished surface instead of P1200 SiC polished). First, an AFM-IR spectrum was obtained for the treated surface (Figure 2d, red line) to identify a frequency that could be attributed to the NHC layer (an AFM-IR spectrum of the untreated surface can be found in Figure S11, including the spectra in Figure 2d for reference). For comparison, the FTIR spectrum of bulk ^{iPr}**NHC·H$_2$CO$_3$** powder (Figure 2d, orange line) and the DFT-predicted spectrum of that same compound (Figure 2d, blue line) are also presented (full spectra in Figure S12). While DFT-predicted frequencies are typically less accurate for crystalline compounds, they provide a general reference for identifying key vibrational modes.

Although the AFM-IR spectrum for the treated surface differs from that of the bulk powder, it remains consistent with the presence of an organic overlayer. In bulk, a C−N stretching frequency is observed at 1247 ± 4 cm^{-1}, assigned based on the DFT simulation and literature data on benzimidazolium compounds.[37,49,50] For the treated surface, we tentatively assign the peak at 1264 ± 1 cm^{-1} to a shifted C−N stretch corresponding to surface-bound NHC. To further explore the surface distribution, an AFM-IR map was generated by tuning the IR laser to 1264 cm^{-1} (Figure 2e). With higher spatial resolution (<10 nm)[51] than ToF-SIMS (<50 nm, but 3.9 μm in this case),[52] the AFM-IR map highlights the nanoscale heterogeneity of the NHC-surface coverage on MiS.

2.3. XPS Analysis of ^{iPr}NHC-Modified Mild Steel. Next, we employed XPS analysis to observe speciation changes on the MiS surface after functionalization. X-ray photoelectron (XP) spectra of the bulk ^{iPr}**NHC·H$_2$CO$_3$** powder (N 1s, C 1s, and O 1s), MiS control (N 1s, C 1s, and Fe 2p), and 5 mM NHC-deposited MiS (N 1s, C 1s, O 1s, and Fe 2p) were collected. The N 1s signal was below the limit of detection (LOD) for the unfunctionalized control MiS sample. The N 1s high-resolution spectra of the bulk powder and NHC-deposited MiS revealed one major signal at 401.0 eV along with a small shoulder at 399.0 eV, which may be attributed to X-ray induced NHC degradation products or other N-

https://doi.org/10.1021/acs.chemmater.4c01804
Chem. Mater. 2025, 37, 76−86

containing products (Figure 3 left column, Table S7). Upon deposition on MiS, the NHC nitrogen signal shifts to 401.8 eV. Interestingly, the peak originally at 399.0 eV also moves upward by 0.8 eV upon deposition. A peak at 401.8 eV indicates degradation products of the alkyl ammonium type NR_4^+.[53,54] These spectra, hence, likely show reaction products rather than NHC bound to the metal or oxide.

The C 1s high-resolution spectra showed peaks originating from air contamination (adventitious carbon, AdC) and the organic compounds of interest. High-resolution C 1s XP spectra were fit according to a previous report on fitting AdC[55] and NHC fitting parameters derived from fitted bulk **^{iPr}NHC** spectra (see Supporting Information, Tables S8, S9 and Figure S13 for detailed XPS fittings and fitting parameters). The C 1s XP spectra confirmed the presence of **^{iPr}NHC** on NHC-modified MiS as well as in the reference, bulk **^{iPr}NHC** powder (Figure 3 middle column). Aside from AdC, the C 1s high-resolution XP spectra of the MiS control detected carbonate (from iron carbonate, determined by Fe 2p XP spectra), which was absent on the NHC-modified MiS.

High-resolution Fe 2p XP spectra were fit according to literature reports (see Figure S14 for detailed XPS fitting).[56] Analysis of the Fe 2p XP spectra of unmodified MiS samples revealed that the carbonate can be attributed to $FeCO_3$, which was absent on the NHC-modified MiS (Figure 3 right column). The two possible justifications for the absence of $FeCO_3$ on the **^{iPr}NHC**-modified MiS are (1) without NHC-modification, the MiS undergoes CO_2 corrosion, forming $FeCO_3$ as a corrosion product,[57] or (2) the NHC reduces all $FeCO_3$ in the deposition process, cleansing it from the NHC-modified MiS surface. At this time, we are not able to differentiate between these two possibilities. For both the control and NHC-modified MiS, Fe_2O_3, Fe_3O_4, and FeO were observed in the oxide layer (Figure 3 right column). A lower amount of iron oxide was observed for the NHC-modified MiS compared to the control, as indicated by the decrease in signal-to-noise ratio and increased metallic-to-oxide Fe 2p peak ratio (Figure 3 bottom right square). A peak at 708.2 eV has been assigned by others[45] to a Fe−C signal resulting from the interaction between NHC and FeO_x wafers. However, in our case, no shift in the Fe 2p peak was observed in the presence of NHC. This may be because this signal is obscured by the stronger metallic Fe signal.

The high-resolution XP spectra for bulk **^{iPr}NHC·H_2CO_3** showed peaks for organic oxides (see Figure S15i for detailed XPS fitting). The O 1s XP spectra of the control and modified MiS samples reflected their respective Fe 2p XP spectra, with lattice oxide and hydroxide peaks appearing for both and a $FeCO_3$ peak only appearing for the unmodified MiS (see Figure S15ii,iii for detailed XPS fitting), agreeing with the C 1s and Fe 2p XP spectra.

2.4. Quantifying Oxide Reduction by ^{iPr}NHC Using Angle-Resolved XPS. To quantify oxide changes, angle-resolved XPS (ARXPS) analyses were carried out using mirror-polished MiS coupons. ARXP spectra were measured at tilt angles of 0° for the control MiS (Figure 4a), 0, 30, and 45° for 5 mM **^{iPr}NHC**-deposited MiS (Figure 4b), and 0, 30, 45, and 60° for 20 mM **^{iPr}NHC**-deposited MiS (Figure 4c). Using the same C 1s fitting parameters for XPS analysis, a higher amount of NHC was observed for 20 mM than 5 mM NHC-modified MiS at all tilt angles, as expected. This was consistent with findings from the N 1s spectra (see Figure S16 and Table S10 for N 1s ARXPS details). As the tilt angle was increased,

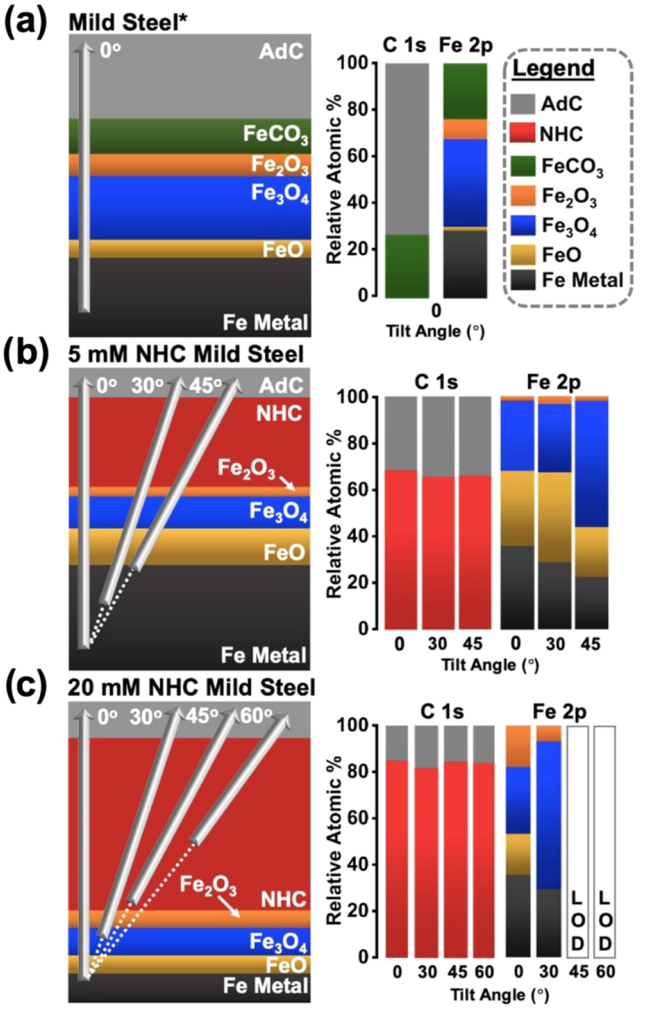

Figure 4. Schematic layering of (a) 0, (b) 5, and (c) 20 mM **^{iPr}NHC**-modified MiS samples accompanied by their respective C 1s and Fe 2p speciation composition at varying tilt angles (AdC = adventitious carbon, LOD = limit of detection). *The layering for (a) has not been defined because only the 0° tilt angle was measured, but it is assumed in this order due to 5 and 20 mM NHC-deposited MiS ARXPS measurements.

resulting in higher surface sensitivity, a decrease in the overall Fe peak intensity was observed, confirming the presence of a carbon-rich top layer for the 5 and 20 mM NHC-deposited MiS samples (see ARXP spectra in Figure S16). The relative amount of NHC does not significantly vary with increasing tilt angles, which is also indicative of a carbene overlayer. Due to the presence of the NHC overlayer, Fe 2p XP spectra could not be collected at 45° and 60° tilts for the 20 mM sample.

Since **^{iPr}NHC** is known to decrease copper oxide prior to functionalization,[21] we examined the ability of **^{iPr}NHC** to decrease surface iron oxide as well. Using Fe 2p XP spectra, the oxide thickness, as determined from the oxide-to-metal ratio and known mean free paths,[58,59] was calculated to be 2.7 ± 0.1 nm for the control, 2.2 ± 0.1 nm for the 5 mM NHC-modified MiS, and 2.3 ± 0.1 nm for the 20 mM NHC-modified MiS. Oxide thickness calculations from the free mean paths were independent of the data set (which tilt value) used, increasing their reliability. Overall, **^{iPr}NHC** was found to interact with and slightly reduce the oxide layer by at least 0.4 nm (15%), consistent with results obtained with Cu.[21] Although no peaks

https://doi.org/10.1021/acs.chemmater.4c01804
Chem. Mater. 2025, 37, 76−86

(N 1s and Fe 2p) associated with Fe-NHC nor Fe−O−NHC were observed by (AR)XPS, the decrease in oxide thickness is attributed to reduction by NHC as the deposition of NHC resulted in the disappearance of $FeCO_3$.

2.5. Electrochemical Characterization of the ^{iPr}NHC Layer on Mild Steel. To determine whether the ^{iPr}NHC layer provided additional corrosion resistance for the MiS surface, electrochemical impedance spectroscopy (EIS) and potentiodynamic polarization (PDP) measurements were carried out. Each electrochemical measurement was done in 3.5 wt % NaCl with ultrapure water. Before each EIS or PDP measurement, the surface was given 30 min to stabilize in the electrolyte at open circuit potential (OCP).

EIS measurements confirmed an increase in corrosion resistance after NHC deposition on MiS. The increase in charge transfer resistance is observed in the Nyquist plot in Figure 5a by the larger magnitude of the NHC-modified MiS

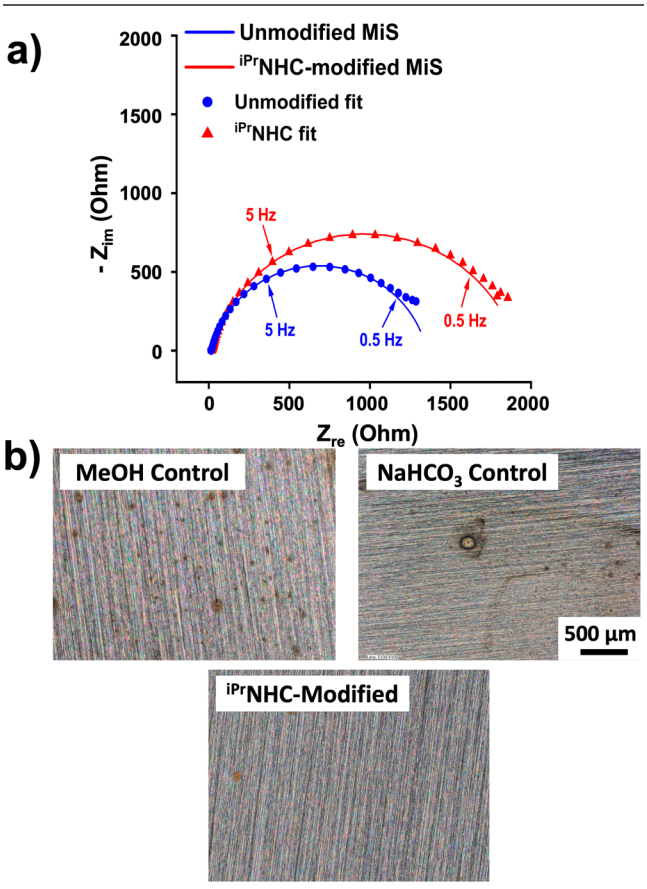

Figure 5. (a) Nyquist plots of unmodified (blue) and ^{iPr}**NHC**-modified (red) mild steel. The symbols (i.e., squares and triangles) indicate the raw data and the solid lines are the respective fittings. The exposed surface area for all samples during electrochemical measurements was 1 cm². (b) Digital microscopy images of MeOH control, $NaHCO_3$ control, and ^{iPr}**NHC**-modified mild steel coupons. The striation, observed for every variation, is a result of polishing with a P1200 SiC paper (i.e., polish lines).

compared to the unmodified control (EIS fitting details and calculated resistance values can be found in Figure S2 and Table S11). PDP measurements also showed a slight improvement in corrosion resistance by a positive shift in the corrosion potential after NHC deposition, consistent with EIS results (PDP plots and fitting details are found in Figure S17 and Table S12, respectively).

The stability of the NHC layer was also evaluated by an international American Society for Testing and Materials (ASTM) standard-based test, where the samples were immersed in 3.5 wt % NaCl for 1 h at room temperature.[60] After 1 h, the MiS coupons were removed from the salt solution, dried, and immediately imaged by digital microscopy. The digital microscope images of varying corrosion artifacts (CAs) on each coupon are shown in Figure 5b.

Both MeOH and $NaHCO_3$ controls displayed dark corrosion artifacts (CAs). Although the corrosion observed on the MeOH control was more widespread than that of the $NaHCO_3$ control, the $NaHCO_3$ control had a higher surface density of CAs due to the larger size of CAs (calculated surface density values in Table S13). The ^{iPr}**NHC**-modified MiS was the least corroded with only a few CAs, demonstrating the deposited ^{iPr}**NHC** as a protective layer.

3. CONCLUSIONS

The use of NHC ligands to modify the surface of mild steel was demonstrated with N,N-diisopropylbenzimidazolylidene (^{iPr}**NHC**) deposited from its carbonic acid salt. Successful functionalization of MiS using an immersion-deposition method was confirmed by MALDI, ToF-SIMS, AFM-IR, and XPS analysis. Using ToF-SIMS surface maps of ^{iPr}**NHC**$^+$ and Fe^+ ions, we observed a thin, widespread NHC layer and found this overlayer to be heterogeneous on the nanoscale by AFM-IR mapping. Using angle-resolved XPS, the NHC was found to reduce a portion (0.4 nm or 15%) of the oxide layer and alter its composition after modification. Corrosion tests in 3.5 wt % NaCl revealed the potential of the NHC modification as a protective layer due to the observed increase in corrosion resistance upon deposition. Our study sets the groundwork for developing more NHC-functionalized Fe-based alloys.

4. EXPERIMENTAL METHODS

4.1. Materials. Mild steel (MiS), SSAB Form 200, from SSAB AB (Borlänge, Sweden), with a 1 mm thickness was used as the main substrate. The MiS composition and mechanical properties are given in Tables S1 and S2. Stainless steel 304 (SS 304) obtained from Outokumpu Nirosta GmbH (Krefeld, Germany), with a 1 mm thickness, was used for ToF-SIMS experiments. The SS 304 composition and mechanical properties are given in Tables S3 and S4. High-strength steel (HSS) obtained from SSAB AB (Borlänge, Sweden), with a 1 mm thickness, was used for ToF-SIMS experiments. The HSS composition and mechanical properties are given in Tables S5 and S6. MiS, SS 304, and HSS sheets were cut into 10 mm × 10 mm coupons, 15 mm × 15 mm coupons, and 18 mm × 18 mm coupons. SiC polishing pads (P800, P1200, and P4000), MD-Pan, MD-Mol, and MD-Nap clothing pads, and DiaPro diamond suspension (9, 3, and 1 μm) were purchased from Struers. 80-grit alumina particles (Al_2O_3) were purchased from the Ruddock Company. For electrochemical tests, a flat electrochemical cell (including a Pt counter electrode) purchased from Ametek (model K0235) was used, along with a saturated calomel electrode (SCE) purchased from Gamry. 2-Nitro-4-(trifluoromethyl) aniline was purchased from Alfa Aesar; chloroform-*d*, and methanol-d_4 were purchased from Sigma-Aldrich.

4.2. General Method for the Synthesis of the NHC Precursor. Reactions were performed in flame-dried flasks with reagent-grade solvents with the exception of CH_2Cl_2 and pentanes, which were distilled from calcium hydride prior to use. Workup purifications were performed using commercial reagent-grade solvents.

https://doi.org/10.1021/acs.chemmater.4c01804
Chem. Mater. 2025, 37, 76−86

4.3. Synthesis of 1,3-Diisopropylbenzimidazolium Iodide. In a pressure tube, benzimidazole (11.84 g, 100 mmol, 1 equiv), K_2CO_3 (20.80 g, 150 mmol, 1.5 equiv), and acetonitrile (200 mL) were added. 2-Iodopropane (31 mL, 300 mmol, 5 equiv) was slowly added, and the flask was sealed and stirred at 90 °C for 48 h. The reaction mixture was allowed to cool to room temperature and was then transferred to a round-bottom flask and the solvent was removed. Dichloromethane was added until just dissolved, and diethyl ether was added to precipitate solid. The solid was collected and washed with ether followed by subsequent drying under high vacuum to afford the desired colorless powder (79.4% yield, 25.2 g). **^{1}H NMR ($CDCl_3$, 700 MHz)**: δ 10.92 (s, 1H), 7.81 (dd, J = 6.23, 3.15 Hz, 2H), 7.65 (dd, J = 6.30, 3.08 Hz), 5.21 (sept, J = 6.79 Hz, 2H), 1.87 (d, J = 6.86 Hz, 12H). **^{13}C NMR (CDCl3, 700 MHz)**: δ 139.62, 130.78, 127.04, 113.94, 52.45, 22.23. **CHN**: Calculated for $C_{13}N_2H_{19}I$: C: 47.29, H: 5.80, N: 8.48 Found: C: 47.75, H: 5.82, N: 8.59 **ESI-MS**, calculated (m/z) for $[C_{13}N_2H_{19}]^+$: 203.15; found: 203.17

4.4. Synthesis of 1,3-Diisopropylbenzimidazolium Bicarbonate. Resin-HCO_3 (200 mL, 3 equiv) suspended in water was measured in a graduated cylinder and transferred to a 100 mL round-bottom flask, where the resin was allowed to settle, and water was decanted off. The resin was washed with methanol three times. 1,3-Diisopropylbenzimidazolium iodide (16.5 g, 50.0 mmol, 1 equiv) was dissolved in methanol (250 mL) and transferred to the resin. The mixture was stirred for 1 h. The solution was passed through a cotton plug and washed with methanol. The solvent was evaporated by air stream and the crude oily product was triturated in acetone and diethyl ether (1:1). The solvent was decanted, and trituration was repeated. Subsequent drying under high vacuum afforded white powder of product (57.0% yield, 7.56 g). **^{1}H NMR** ($CDCl_3$, 700 MHz): δ 8.07 (dd, J = 6.3, 3.2 Hz, 2H), 7.75 (dd, J = 6.3, 3.1 Hz, 2H), 5.11 (sept, J = 6.7 Hz, 2H), 1.77 (d, J = 6.7 Hz, 12H). **^{13}C NMR** ($CDCl_3$, 700 MHz): δ 161.42, 138.96, 132.59, 128.19, 114.97, 52.83, 22.11. **CHN:** Calculated for $C_{14}N_2O_3H_{20}$: C: 63.62, H, 7.63, N: 10.60 Found: C: 62.41, H: 7.67, N: 10.31

4.5. Mild Steel Surface Preparation. MiS coupons were polished with P1200 SiC polishing pads using a Struers TegraForce-5 polishing machine until the surface was visibly smooth and uniform.

For atomic force microscopy-based infrared spectroscopy (AFM-IR) and angle-resolved X-ray photoelectron spectroscopy (ARXPS) analysis, coupons were polished with the following sequence of SiC polishing pads; P800, P1200, and P4000, using a Struers TegraForce-5 polishing machine until the surface was visibly smooth and uniform. Then, using MD-Pan, MD-Mol, and MD-NAP cloth pads, the surface was further polished with 9, 3, and 1 μm diamond suspension, respectively, to get a mirror-finish surface. The 10 × 10 mm coupons were used for both procedures.

To optimize the immersion-deposition method based on the effects of surface roughness, two more surface variations were introduced: as-received (AR) and sandblasted (SB). To obtain the SB variation, a grit-blaster (ECO 420—Sandblasting Cabinet for Light-Duty Applications, International Surface Technologies) with 80-grit alumina particles (Al_2O_3) was used. The AR variation was achieved by leaving the coupons as received without abrasion.

After the surface was prepared with one of the above-mentioned methods, coupons were cleaned for 10 min in acetone followed by 10 min in isopropanol using a sonicator (Branson 2510). Subsequently, the coupons were dried with nitrogen gas.

4.6. Stainless Steel 304 Surface Preparation. Stainless steel 304 (SS 304) coupons were polished with SiC papers (800, 1200, and 4000), followed by aluminum polishing (0.05 μm) using a Struers TegraForce-5 polishing machine until the surface was visibly mirror-polished. After polishing, the coupons were cleaned ultrasonically in acetone, followed by isopropanol for 10 min each. Then, the coupons were dried with nitrogen gas at room temperature and left in a desiccator until deposition. Before NHC deposition, the coupons were cleaned again ultrasonically (following the above-mentioned steps).

4.7. High Strength Steel Surface Preparation. High strength steel (HSS) coupons (as-received) were cleaned ultrasonically in 2-propanol followed by acetone for 10 min each. Then, coupons were dried with nitrogen gas.

4.8. Immersion-Deposition Method. Following surface preparation, the coupons were placed directly into fresh 5 mM ^{iPr}NHC·H_2CO_3 in MeOH solution and immersed for 24 ± 0.5 h. The coupons were placed with their to-be-modified faces facing upward.

After the 24 h immersion period, coupons were removed from solution, placed in a clean Petri dish, and rinsed with 4 × 15 mL of MeOH by swirling the coupons around for 1 min each time. After being rinsed, the coupons were dried with a direct stream of nitrogen gas and stored in a desiccator at room temperature.

The control (or reference) coupons were subject to the same conditions but with pure MeOH (no ^{iPr}NHC·H_2CO_3). The coupons were directly dried with nitrogen gas after the 24 h immersion and stored in a desiccator at room temperature.

For ARXPS analysis, the immersion-deposition methods were repeated using 20 mM ^{iPr}NHC·H_2O_3. This provided concentration-dependent information about the thickness of the deposited layer and MiS surface interactions by ARXPS.

4.9. Scanning Electron Microscopy−Energy Dispersive X-ray Spectroscopy (SEM−EDX). SEM−EDX analysis was carried out using a FEI Quanta 450 FE-SEM coupled with an EDAX Octane Super 60 mm^2 SDD and TEAM EDS Analysis System. Each analyzed coupon was adhered to the stage using double-sided carbon tape and was analyzed using secondary electrons with an accelerating voltage of 10 kV, a spot size of 2.5 nm, and a dwell time of 300 ns. The EDX analysis was done by using point analysis.

4.10. X-ray Photoelectron Spectroscopy (XPS). XPS analysis was carried out using a Thermo Fisher Scientific K-α X-ray Photoelectron Spectrometer and a monochromatic Al K(α) source. Single point analysis was performed on each coupon, collecting a survey spectrum (5 scans, pass energy, PE of 200 eV) and four high-resolution spectra of C 1s, O 1s, N 1s, and Fe 2p (10 scans each, pass energy of 50 eV). Each spectrum was analyzed and fit by using version 6.5.0 of the Avantage Surface Chemical Analysis software by Thermo Scientific. All scans were charge-corrected using the adventitious carbon (C 1s), with a binding energy (BE) of 284.8 eV. The survey scan was fitted using the automatic ID function. The peaks in the high-resolution spectra were fitted using the Smart peak background function, a Convolve Gaussian−Lorentzian mix, and a Powell fitting algorithm.

Another set of XPS measurements was performed using a Kratos AXIS Supra Spectrometer with a monochromatic Al Kα source (15 mA, 15 kV). Instrument work functions were calibrated to give Au $4f_{7/2}$ metallic gold BE of 83.96 eV. The base pressure of the instrument was 8 × 10^{-10} Torr. The survey scan spectra were collected with an analysis area of approximately 300 μm × 700 μm at a 160 eV pass energy (PE). High-resolution analyses were carried out with an analysis area of 300 μm × 700 μm at 20 eV PE. The Kratos charge neutralizer system was used on all specimens, which were electrically isolated (floated). High-resolution C 1s, O 1s, N 1s, and -Fe 2p were collected. All spectra were charge-corrected to the aliphatic carbon signal at a BE of 284.8 eV (adventitious carbon, C−H, C−C on sample) and analyzed using CasaXPS software (version 2.3.2.6) with a Shirley background.

During bulk NHC measurements, the ^{iPr}NHC·H_2CO_3 powder was electrically isolated from the stage to obtain a constant surface potential. A copper tape masking technique was used to further improve the charge neutralization of the samples. To investigate peak changes originating from ultrahigh vacuum and X-ray exposure and subsequent heat generated from X-ray exposure, timed degradation studies of the ^{iPr}NHC·H_2CO_3 powder were carried out on one sample spot for 10 h (one measurement per hour). During each hour, the spectra were collected for 40 min and no spectrum was collected in the remaining 20 min.

4.11. Angle-Resolved X-ray Photoelectron Spectroscopy (ARXPS). The ARXPS experiments were completed by using a Kratos AXIS Supra Spectrometer with a monochromatic Al Kα source (15

https://doi.org/10.1021/acs.chemmater.4c01804
Chem. Mater. 2025, 37, 76−86

mA, 15 kV). Electrostatic mode was used throughout, and the samples were measured at 0, 30, 45, and 60° tilt angles.

4.12. Time-of-Flight Secondary Ion Mass Spectrometry (ToF-SIMS). ToF-SIMS measurements were performed with an ION-TOF-SIMS IV instrument on five different spots on each metal coupon. A pulsed 25 keV Bi_3^+ cluster primary ion beam was used to bombard the sample surface to generate secondary ions. A pulsed, low-energy electron flood was used to neutralize the sample charging. Ion mass spectra were collected in an area of 500 μm × 500 μm at 128 × 128 pixels (3.9 μm per pixel). Normalization intensities of ions to the total ion intensity were used.

The measurements were performed on unmodified, 5 and 20 mM NHC-modified mild steel coupons. To compare the thermal stabilities of the two different NHCs, the NHC-modified coupons were further exposed to 100 °C for 1 h in air, followed by further rinsing and ToF-SIMS measurements.

To determine the surface coverage of the NHC from mapping, an arbitrary cutoff pixel value was used.

4.13. Matrix-Assisted Laser Desorption/Ionization Time-of-Flight Mass Spectrometry (MALDI ToF-MS). MALDI ToF-MS analysis was carried out by using a Bruker Autoflex III Smart Beam MALDI ToF Mass Spectrometer. A Nd:YAG laser with a wavelength of 355 nm and a laser pulse of 5 ns was used. The acquisition method used was a positive reflector mode. To analyze the surface of the coupons directly, a custom three-dimensional (3D)-printed sample holder of poly(ethylene terephthalate) glycol was made. Although the instrument abbreviation MALDI is used throughout the text, no matrix was used.

4.14. Atomic Force Microscopy with Infrared Spectroscopy (AFM-IR). The Anasys nanoIR2 spectrometer equipped with a pulsed tunable QCL laser (900−1900 cm^{-1}) was utilized to collect AFM-IR data on MiS coupons. Contact-mode AFM-IR analysis was performed with a precalibrated (using a test sample) gold cantilever. The chemical map, which reveals the distribution of ^{iPr}NHC over the surface was obtained by tuning the AFM-IR laser with C−N stretching frequency at 1264 cm^{-1}. Subsequently, the signal power was optimized by pulse tuning the signal to improve intensities and avoid split signals to obtain IR absorption spectra at the nanoscale of the sample. AFM-IR spectra were collected with 1 cm^{-1} spectral resolution. All data was collected and treated using the Analysis Studio (version 3.15) software.

4.15. Fourier Transform Infrared Spectroscopy (FTIR). A Spectrum II FTIR spectrophotometer from PerkinElmer was utilized to record the IR spectrum of the ^{iPr}NHC·H_2CO_3 powder. Spectra were collected at a resolution of 4 cm^{-1}.

4.16. Nuclear Magnetic Resonance (NMR) Spectroscopy. ^{1}H and ^{13}C NMR spectra were recorded on a Bruker Instruments (Neo-600) operating at denoted spectrometer frequency given in megahertz (MHz). ^{1}H chemical shifts are referenced to the residual protons of the deuterated solvents $CDCl_3$ (at δ = 7.26 ppm) and CD_3OD (at δ = 3.31 ppm); ^{13}C chemical shifts are referenced to the $CDCl_3$ and CD_3OD signals at δ = 77.16 and 49.00 ppm, respectively. The following abbreviations are used to describe NMR signals: s = singlet, d = doublet, t = triplet, q = quartet, sept = septet, and m = multiplet. All data was processed using MestReNova 11.0 software.

4.17. Digital Microscopy. To image the samples before and after undergoing stability testing in 3.5 wt % NaCl, a Keyence VHX-7000/7000N Microscope was used. The 200−2000 magnification lens was used with full-ring or partial-ring. To enhance the image quality, the "Increase Image Quality" function was chosen.

4.18. Density Functional Theory (DFT) Calculations. All DFT calculations were performed using the Gaussian 16 suite.[61] Geometries and frequency calculations were done at the B3LYP-D3/6-311+G(2d,2p)[62,63] level of theory in SMD[64] implicit solvent model for CH_3CN. After optimization, ground states were confirmed to be local minima by the absence of imaginary frequencies. Thermodynamic functions were calculated for the default temperature of 298.15 K and a pressure of 1 atm. For the simulated spectra, the harmonic frequencies were scaled by a factor of 0.97 to account for anharmonicity. Peak broadening was simulated in the software GaussView[65] using a half-width at half height of 4 cm^{-1}.

4.19. Open Circuit Potential (OCP) Measurements. OCP was run on a BioLogic potentiostat for a total of 30 min in 3.5 wt % NaCl solution before each potentiodynamic polarization and electrochemical impedance spectroscopy measurement.

4.20. Electrochemical Impedance Spectroscopy (EIS) Measurements. All EIS measurements were carried out using galvanostatic mode in 3.5 wt % NaCl solution using a Biologic potentiostat. A frequency range of 1 mHz to 1 MHz was used, along with a sinus amplitude of 10 mV. Fitting procedure and equivalent circuits are given in the Supporting Information.

4.21. Potentiodynamic Polarization Measurements. PDP measurements were performed on unmodified and ^{iPr}NHC-deposited MiS coupons in 3.5 wt % NaCl solution to determine their corrosion potentials. The initial potential was set to −0.3 V vs the prior measured OCP, with a scan rate of 0.5 mV/s, and a final potential of 1 V (vs the reference calomel electrode). The measurement was often stopped before reaching the final potential if a steady plateau (∼55−65 mA) was achieved. Tafel fitting was carried out using the Tafel fit function in EC-Lab software (version 11.50) to determine the corrosion potential.

4.22. Salt Immersion Test and Corrosion Artifact Density Calculations. NHC-modified and unmodified (MeOH control) MiS coupons were immersed in 50 mL of 3.5 wt % NaCl solution in lidded jars for 1 h at RT. After 1 h, the coupons were removed from the solution, dried with a controlled stream of air, and imaged by a Keyence digital microscope. To calculate the density of corrosion artifacts (CA) on the surface, digital microscope images were converted to gray scale and Otsu thresholding[66] was used to segment the pits from the steel throughout the image. Groups of segmented pixels were labeled as 'pits' and were counted. The corrosion artifact density (CA/mm^2) was calculated for each image by dividing the number of "pits" by the image area in millimeters squared. Custom code written in Python (version 3.12) was used for all image processing and the Python library called, "OpenCV" (version 4.10.0-dev) was used for Otsu thresholding.[67]

■ ASSOCIATED CONTENT

Supporting Information

The Supporting Information is available free of charge at https://pubs.acs.org/doi/10.1021/acs.chemmater.4c01804.

Detailed experimental methods, optimization procedures, full range of the MS spectra, degradation study during XPS analysis, TGA results, and *XYZ* coordinates of the DFT-calculated structures (PDF)

■ AUTHOR INFORMATION

Corresponding Authors

Mark Biesinger − *Department of Chemistry, Western University, London, Ontario N6A 5B7, Canada; Surface Science Western, London, Ontario N6G 0J3, Canada; Carbon to Metal Coating Institute, Queen's University, Kingston, Ontario K7L 3N6, Canada*; Email: biesingr@uwo.ca

James J. Noel − *Department of Chemistry, Western University, London, Ontario N6A 5B7, Canada; Surface Science Western, London, Ontario N6G 0J3, Canada; Carbon to Metal Coating Institute, Queen's University, Kingston, Ontario K7L 3N6, Canada*; Email: jjnoel@uwo.ca

Yolanda S. Hedberg − *Department of Chemistry, Western University, London, Ontario N6A 5B7, Canada; Surface Science Western, London, Ontario N6G 0J3, Canada; Carbon to Metal Coating Institute, Queen's University, Kingston, Ontario K7L 3N6, Canada*; orcid.org/0000-0003-2145-3650; Email: yhedberg@uwo.ca

https://doi.org/10.1021/acs.chemmater.4c01804
Chem. Mater. 2025, 37, 76−86

Cathleen M. Crudden − *Carbon to Metal Coating Institute, Queen's University, Kingston, Ontario K7L 3N6, Canada; Department of Chemistry, Queen's University, Kingston, Ontario K7L 3N6, Canada; Institute of Transformative Bio-Molecules (WPI-ITbM), Nagoya University, Nagoya 464-8602, Japan;* orcid.org/0000-0003-2154-8107; Email: cruddenc@chem.queensu.ca

Janine Mauzeroll − *Department of Chemistry, McGill University, Montreal, Quebec H3A 0B8, Canada; Carbon to Metal Coating Institute, Queen's University, Kingston, Ontario K7L 3N6, Canada;* orcid.org/0000-0003-4752-7507; Email: janine.mauzeroll@mcgill.ca

Authors

Lila Laundry-Mottiar − *Department of Chemistry, McGill University, Montreal, Quebec H3A 0B8, Canada; Carbon to Metal Coating Institute, Queen's University, Kingston, Ontario K7L 3N6, Canada*

Thilini Malsha Suduwella − *Department of Chemistry, McGill University, Montreal, Quebec H3A 0B8, Canada; Carbon to Metal Coating Institute, Queen's University, Kingston, Ontario K7L 3N6, Canada*

Waruni G. K. Senanayake − *Department of Chemistry, Western University, London, Ontario N6A 5B7, Canada; Carbon to Metal Coating Institute, Queen's University, Kingston, Ontario K7L 3N6, Canada*

Matthew J. Turnbull − *Department of Chemistry, Western University, London, Ontario N6A 5B7, Canada; Carbon to Metal Coating Institute, Queen's University, Kingston, Ontario K7L 3N6, Canada;* orcid.org/0000-0002-4661-8872

Antoine Juneau − *Department of Chemistry, McGill University, Montreal, Quebec H3A 0B8, Canada; Carbon to Metal Coating Institute, Queen's University, Kingston, Ontario K7L 3N6, Canada;* orcid.org/0000-0001-9207-8013

Ekrupe Kaur − *Department of Chemistry, Western University, London, Ontario N6A 5B7, Canada; Carbon to Metal Coating Institute, Queen's University, Kingston, Ontario K7L 3N6, Canada*

Mark D. Aloisio − *Carbon to Metal Coating Institute, Queen's University, Kingston, Ontario K7L 3N6, Canada; Department of Chemistry, Queen's University, Kingston, Ontario K7L 3N6, Canada*

Thiago M. Guimarães Selva − *Department of Chemistry, McGill University, Montreal, Quebec H3A 0B8, Canada; Carbon to Metal Coating Institute, Queen's University, Kingston, Ontario K7L 3N6, Canada; Federal institute of Rio de Janeiro, Rio de Janeiro, RJ 20271-021, Brazil*

Jeffrey D. Henderson − *Surface Science Western, London, Ontario N6G 0J3, Canada*

Heng-Yong Nie − *Surface Science Western, London, Ontario N6G 0J3, Canada; Carbon to Metal Coating Institute, Queen's University, Kingston, Ontario K7L 3N6, Canada;* orcid.org/0000-0002-8287-5171

Complete contact information is available at: https://pubs.acs.org/10.1021/acs.chemmater.4c01804

Author Contributions

L.L.-M.—Performed MALDI, XPS, EIS, and PDP measurements, as well as salt immersion tests, and corresponding evaluation. Wrote, edited, and created figures for the manuscript. T.M.S.—Performed AFM-IR and IR measurements and evaluation. Edited and created figures for the manuscript. W.S.—Performed ToF-SIMS and ToF-SIMS map measurements and evaluation. Edited the manuscript. M.J.T.—Performed ARXPS measurements and fitting. Oxide thickness calculations. Edited the manuscript. A.J.—Performed DFT simulations and edited the manuscript. E.K.—Developed bulk NHC peak fitting parameters used in C 1s spectra. Edited the manuscript. M.D.A.—Synthesized several batches of ^{iPr}NHC for deposition. Created figures and edited the manuscript. T.M.G. S.—Provided guidance on SS 304 measurements. J.D.H.—Assisted with ARXPS fittings and evaluation. H.-Y.N.—Assisted with ToF-SIMS measurements, training, and evaluation. Edited the manuscript. M.B.—Reviewed (AR) XPS fittings and oxide thickness calculations. Edited the manuscript. J.J.N.—Performed supervision and edited the manuscript. Y.S.H.—Performed conceptualization, supervision, editing, and reviewing related to the ToF-SIMS, XPS, and electrochemical measurements and evaluation. C.M.C.—Performed conceptualization, supervision, editing, and reviewing the manuscript and data analysis/interpretation. J.M.—Performed conceptualization, supervision, editing, and reviewing the manuscript and data analysis/interpretation. The manuscript was written through contributions of all authors. All authors have given approval to the final version of the manuscript.

Notes

The authors declare no competing financial interest.

■ ACKNOWLEDGMENTS

This work was financially supported by NFRF Canada (NFRFT-2020-00573, grant recipient: C.M.C.), the Canada Research Chairs Program (CRC-2019-00425, grant recipient: Y.S.H.), the Canada Foundation for Innovation (Innovation Fund 35961, grant recipient: M.B.), and the Wolfe-Western Fellowship program (2020, grant recipient: Y.S.H.). The authors thank Dr. Emily Albright for all her support and team organization. The authors thank Nadim K. Saadé for assistance with MALDI measurements and Dr. Yuanjiao Li for research support (McGill University). We extend our gratitude to Patricia Morale, the AFM core facility manager at the Laboratoire de Caractérisation des Matériaux, Université de Montréal, for her assistance with the AFM-IR measurements. Access to computational clusters was kindly provided by the Digital Research Alliance of Canada. Dr. Marshall Yang is acknowledged for assistance in the ToF-SIMS measurements. Jonathan Adsetts is gratefully acknowledged for performing the corrosion artifact calculations from digital images.

■ REFERENCES

(1) Buildings and Infrastructure, 2024. worldsteel.org; https://worldsteel.org/steel-topics/steel-markets/buildings-and-infrastructure/.

(2) Schlegel, J. *The World of Steel—On the History, Production and Use of a Basic Material*; Springer, 2023.

(3) Zhang, W.; Xu, J. Advanced Lightweight Materials for Automobiles: A Review. *Mater. Des.* **2022**, *221*, No. 110994.

(4) Koch, G.; Varney, J.; Thompson, N.; Moghissi, O.; Gould, M.; Payer, J. *NACE International Impact Report—International Measures of Prevention, Application, and Economics of Corrosion Technologies Study*; NACE International, 2016.

(5) Iannuzzi, M.; Frankel, G. S. The Carbon Footprint of Steel Corrosion. *npj Mater. Degrad.* **2022**, *6* (1), 1−4.

(6) Basu, S. N. Thermal and Environmental Barrier Coatings for Si-Based Ceramics. In *Comprehensive Hard Materials*; Sarin, V. K., Ed.;

Elsevier: Oxford, 2014; Chapter 2.17, pp 469−489. DOI: 10.1016/B978-0-08-096527-7.00036-2.
(7) Amirudin, A.; Thieny, D. Application of Electrochemical Impedance Spectroscopy to Study the Degradation of Polymer-Coated Metals. *Prog. Org. Coat.* **1995**, *26* (1), 1−28.
(8) González-García, Y.; González, S.; Souto, R. M. Electrochemical and Structural Properties of a Polyurethane Coating on Steel Substrates for Corrosion Protection. *Corros. Sci.* **2007**, *49* (9), 3514−3526.
(9) Kausar, A. Advances in Anti-Corrosive Coatings of Polymer/Graphene Nanocomposites. In *Graphene to Polymer/Graphene Nanocomposites*; Kausar, A., Ed.; Elsevier, 2022; Chapter 7, pp 145−172. DOI: 10.1016/B978-0-323-90937-2.00006-X.
(10) Xue, X.; Lu, J. Electrochemical Impedance Spectroscopy Investigation of a Polyurethane Coating on Bridge 16Mnq Steel Surface. *Int. J. Electrochem. Sci.* **2017**, *12* (4), 3179−3187.
(11) Farh, H. M. H.; Ben Seghier, M. E. A.; Zayed, T. A Comprehensive Review of Corrosion Protection and Control Techniques for Metallic Pipelines. *Eng. Failure Anal.* **2023**, *143*, No. 106885.
(12) Oura, K.; Katayama, M.; Zotov, A. V.; Lifshits, V. G.; Saranin, A. A. Atomic Structure of Surfaces with Adsorbates. In *Surface Science: An Introduction*; Springer: Berlin, Heidelberg, 2003; pp 195−227. DOI: 10.1007/978-3-662-05179-5_9.
(13) Hutchinson, R. G.; Hutchinson, J. W. Lifetime Assessment for Thermal Barrier Coatings: Tests for Measuring Mixed Mode Delamination Toughness. *J. Am. Ceram. Soc.* **2011**, *94* (s1), s85−s95.
(14) Shinde, S. V.; Sampath, S. Interplay between Cracking and Delamination in Incrementally Deposited Plasma Sprayed Coatings. *Acta Mater.* **2021**, *215*, No. 117074.
(15) Fan, C.; Liu, Y.; Yin, X.; Shi, J.; Dilger, K. Electrochemical Behavior and Interfacial Delamination of a Polymer-Coated Galvanized Steel System in Acid Media. *ACS Omega* **2021**, *6* (31), 20331−20340.
(16) Crudden, C. M.; Horton, J. H.; Ebralidze, I. I.; Zenkina, O. V.; McLean, A. B.; Drevniok, B.; She, Z.; Kraatz, H.-B.; Mosey, N. J.; Seki, T.; Keske, E. C.; Leake, J. D.; Rousina-Webb, A.; Wu, G. Ultra Stable Self-Assembled Monolayers of N-Heterocyclic Carbenes on Gold. *Nat. Chem.* **2014**, *6* (5), 409−414.
(17) Jiang, L.; Zhang, B.; Médard, G.; Seitsonen, A. P.; Haag, F.; Allegretti, F.; Reichert, J.; Kuster, B.; Barth, J. V.; Papageorgiou, A. C. N. -Heterocyclic Carbenes on Close-Packed Coinage Metal Surfaces: Bis-Carbene Metal Adatom Bonding Scheme of Monolayer Films on Au, Ag and Cu. *Chem. Sci.* **2017**, *8* (12), 8301−8308.
(18) Lovat, G.; Doud, E. A.; Lu, D.; Kladnik, G.; Inkpen, M. S.; Steigerwald, M. L.; Cvetko, D.; Hybertsen, M. S.; Morgante, A.; Roy, X.; Venkataraman, L. Determination of the Structure and Geometry of N-Heterocyclic Carbenes on Au(111) Using High-Resolution Spectroscopy. *Chem. Sci.* **2019**, *10* (3), 930−935.
(19) Amit, E.; Dery, L.; Dery, S.; Kim, S.; Roy, A.; Hu, Q.; Gutkin, V.; Eisenberg, H.; Stein, T.; Mandler, D.; Dean Toste, F.; Gross, E. Electrochemical Deposition of N-Heterocyclic Carbene Monolayers on Metal Surfaces. *Nat. Commun.* **2020**, *11* (1), No. 5714.
(20) Navarro, J. J.; Das, M.; Tosoni, S.; Landwehr, F.; Bruce, J. P.; Heyde, M.; Pacchioni, G.; Glorius, F.; Roldan Cuenya, B. Covalent Adsorption of N-Heterocyclic Carbenes on a Copper Oxide Surface. *J. Am. Chem. Soc.* **2022**, *144* (36), 16267−16271.
(21) Veinot, A. J.; Al-Rashed, A.; Padmos, J. D.; Singh, I.; Lee, D. S.; Narouz, M. R.; Lummis, P. A.; Baddeley, C. J.; Crudden, C. M.; Horton, J. H. N-Heterocyclic Carbenes Reduce and Functionalize Copper Oxide Surfaces in One Pot. *Chem. - Eur. J.* **2020**, *26* (50), 11431−11434.
(22) Kaur, G.; Thimes, R. L.; Camden, J. P.; Jenkins, D. M. Fundamentals and Applications of N-Heterocyclic Carbene Functionalized Gold Surfaces and Nanoparticles. *Chem. Commun.* **2022**, *58* (95), 13188−13197.
(23) Zhukhovitskiy, A. V.; Mavros, M. G.; Van Voorhis, T.; Johnson, J. A. Addressable Carbene Anchors for Gold Surfaces. *J. Am. Chem. Soc.* **2013**, *135* (20), 7418−7421.
(24) Weidner, T.; Baio, J. E.; Mundstock, A.; Große, C.; Karthäuser, S.; Bruhn, C.; Siemeling, U. NHC-Based Self-Assembled Monolayers on Solid Gold Substrates. *Aust. J. Chem.* **2011**, *64* (8), 1177−1179.
(25) Smith, C. A.; Narouz, M. R.; Lummis, P. A.; Singh, I.; Nazemi, A.; Li, C.-H.; Crudden, C. M. N-Heterocyclic Carbenes in Materials Chemistry. *Chem. Rev.* **2019**, *119* (8), 4986−5056.
(26) Zhukhovitskiy, A. V.; MacLeod, M. J.; Johnson, J. A. Carbene Ligands in Surface Chemistry: From Stabilization of Discrete Elemental Allotropes to Modification of Nanoscale and Bulk Substrates. *Chem. Rev.* **2015**, *115* (20), 11503−11532.
(27) Trujillo, M. J.; Strausser, S. L.; Becca, J. C.; DeJesus, J. F.; Jensen, L.; Jenkins, D. M.; Camden, J. P. Using SERS To Understand the Binding of N-Heterocyclic Carbenes to Gold Surfaces. *J. Phys. Chem. Lett.* **2018**, *9* (23), 6779−6785.
(28) Bakker, A.; Timmer, A.; Kolodzeiski, E.; Freitag, M.; Gao, H. Y.; Mönig, H.; Amirjalayer, S.; Glorius, F.; Fuchs, H. Elucidating the Binding Modes of N-Heterocyclic Carbenes on a Gold Surface. *J. Am. Chem. Soc.* **2018**, *140* (38), 11889−11892.
(29) Park, S.; Kang, S.; Yoon, H. J. Thermopower of Molecular Junction in Harsh Thermal Environments. *Nano Lett.* **2022**, *22* (10), 3953−3960.
(30) Kang, S.; Byeon, S. E.; Yoon, H. J. N-Heterocyclic Carbene Anchors in Electronics Applications. *Bull. Korean Chem. Soc.* **2021**, *42* (5), 712−723.
(31) Dery, S.; Kim, S.; Tomaschun, G.; Berg, I.; Feferman, D.; Cossaro, A.; Verdini, A.; Floreano, L.; Klüner, T.; Toste, F. D.; Gross, E. Elucidating the Influence of Anchoring Geometry on the Reactivity of NO2-Functionalized N-Heterocyclic Carbene Monolayers. *J. Phys. Chem. Lett.* **2019**, *10* (17), 5099−5104.
(32) Crudden, C. M.; Allen, D. P. Stability and Reactivity of *N*-Heterocyclic Carbene Complexes. *Coord. Chem. Rev.* **2004**, *248* (21), 2247−2273.
(33) Hopkinson, M. N.; Richter, C.; Schedler, M.; Glorius, F. An Overview of N-Heterocyclic Carbenes. *Nature* **2014**, *510* (7506), 485−496.
(34) Ruiz-Varilla, A. M.; Baquero, E. A.; Chaudret, B.; Jesús, E. de.; Gonzalez-Arellano, C.; Flores, J. C. Water-Soluble NHC-Stabilized Platinum Nanoparticles as Recoverable Catalysts for Hydrogenation in Water. *Catal. Sci. Technol.* **2020**, *10* (9), 2874−2881.
(35) Ghosh, M.; Khan, S. N-Heterocyclic Carbenes Capped Metal Nanoparticles: An Overview of Their Catalytic Scope. *ACS Catal.* **2023**, *13* (14), 9313−9325.
(36) Berg, I.; Amit, E.; Hale, L.; Toste, F. D.; Gross, E. N-Heterocyclic Carbene Based Nanolayer for Copper Film Oxidation Mitigation. *Angew. Chem., Int. Ed.* **2022**, *61* (25), No. e202201093.
(37) Zeng, Y.; Zhang, T.; Narouz, M. R.; Crudden, C. M.; McBreen, P. H. Generation and Conversion of an N-Heterocyclic Carbene on Pt(111). *Chem. Commun.* **2018**, *54* (88), 12527−12530.
(38) Lee, D. S.; Singh, I.; Veinot, A. J.; Aloisio, M. D.; Lomax, J. T.; Ragogna, P. J.; Crudden, C. M. Mesoionic Carbene-Based Self-Assembled Monolayers on Gold. *Chem. Sci.* **2024**, *15*, 2480−2485, DOI: 10.1039/D3SC04720B.
(39) Dery, S.; Bellotti, P.; Ben-Tzvi, T.; Freitag, M.; Shahar, T.; Cossaro, A.; Verdini, A.; Floreano, L.; Glorius, F.; Gross, E. Influence of N-Substituents on the Adsorption Geometry of OH-Functionalized Chiral N-Heterocyclic Carbenes. *Langmuir* **2021**, *37* (33), 10029−10035.
(40) Inayeh, A.; Groome, R. R. K.; Singh, I.; Veinot, A. J.; de Lima, F. C.; Miwa, R. H.; Crudden, C. M.; McLean, A. B. Self-Assembly of N-Heterocyclic Carbenes on Au(111). *Nat. Commun.* **2021**, *12* (1), No. 4034.
(41) Qie, B.; Wang, Z.; Jiang, J.; Zhang, Z.; Jacobse, P. H.; Lu, J.; Li, X.; Liu, F.; Alexandrova, A. N.; Louie, S. G.; Crommie, M. F.; Fischer, F. R. Synthesis and Characterization of Low-Dimensional N-Heterocyclic Carbene Lattices. *Science* **2024**, *384* (6698), 895−901.
(42) Larrea, C. R.; Baddeley, C. J.; Narouz, M. R.; Mosey, N. J.; Horton, J. H.; Crudden, C. M. N-Heterocyclic Carbene Self-Assembled Monolayers on Copper and Gold: Dramatic Effect of

Wingtip Groups on Binding, Orientation and Assembly. *ChemPhysChem* **2017**, *18* (24), 3536−3539.
(43) Angove, E.; Grillo, F.; Früchtl, H. A.; Veinot, A. J.; Singh, I.; Horton, J. H.; Crudden, C. M.; Baddeley, C. J. Highly Ordered N-Heterocyclic Carbene Monolayers on Cu(111). *J. Phys. Chem. Lett.* **2022**, *13* (8), 2051−2056.
(44) Callister, W. D.; Rethwisch, D. G. *Materials Science and Engineering: An Introduction*; Wiley, 2018.
(45) Amit, E.; Mondal, R.; Berg, I.; Nairoukh, Z.; Gross, E. N-Heterocyclic Carbene Monolayers on Metal-Oxide Films: Correlations between Adsorption Mode and Surface Functionality. *Langmuir* **2024**, *40*, 10374.
(46) Crudden, C. M.; Horton, J. H.; Narouz, M. R.; Li, Z.; Smith, C. A.; Munro, K.; Baddeley, C. J.; Larrea, C. R.; Drevniok, B.; Thanabalasingam, B.; McLean, A. B.; Zenkina, O. V.; Ebralidze, I. I.; She, Z.; Kraatz, H.-B.; Mosey, N. J.; Saunders, L. N.; Yagi, A. Simple Direct Formation of Self-Assembled N-Heterocyclic Carbene Monolayers on Gold and Their Application in Biosensing. *Nat. Commun.* **2016**, *7* (1), No. 12654.
(47) Navarro, J. J.; Das, M.; Tosoni, S.; Landwehr, F.; Koy, M.; Heyde, M.; Pacchioni, G.; Glorius, F.; Roldan Cuenya, B. Growth of N-Heterocyclic Carbene Assemblies on Cu(100) and Cu(111): From Single Molecules to Magic-Number Islands. *Angew. Chem., Int. Ed.* **2022**, *61* (30), No. e202202127.
(48) Muramoto, S.; Brison, J.; Castner, D. G. Exploring the Surface Sensitivity of ToF-SIMS by Measuring the Implantation and Sampling Depths of Bin and C60 Ions in Organic Films. *Anal. Chem.* **2012**, *84* (1), 365−372.
(49) Jamil, S.; Gondal, H. Y.; Ali, A.; Hussain, A.; Akram, N.; Nisar, M.; Tahir, M. N.; Ashfaq, M.; Raza, A. R.; Muhammad, S.; Cheema, Z. M.; Mustafai, A.; Sameeh, M. Y. Benzimidazolium Quaternary Ammonium Salts: Synthesis, Single Crystal and Hirshfeld Surface Exploration Supported by Theoretical Analysis. *R. Soc. Open Sci.* **2024**, *11* (2), No. 231094.
(50) Malek, K.; Puc, A.; Schroeder, G.; Rybachenko, V. I.; Proniewicz, L. M. FT-IR and FT-Raman Spectroscopies and DFT Modelling of Benzimidazolium Salts. *Chem. Phys.* **2006**, *327* (2), 439−451.
(51) Anasys nanoIR3-s, 2024. https://www.bruker.com/en/products-and-solutions/infrared-and-raman/nanoscale-infrared-spectrometers/anasys-nanoir3-s.html.
(52) IONTOF. IONTOF—TOF-SIMS (Time of Flight Secondary Ion Mass Spectrometry)—LEIS (Low Energy Ion Scattering), 2024. https://www.iontof.com/m6-tof-sims-technical-details.html.
(53) Beamson, G.; Briggs, D. *High Resolution XPS of Organic Polymers: The Scienta ESCA300 Database*; John Wiley: Chichester, UK, 1993.
(54) Gorham, J. *NIST X-Ray Photoelectron Spectroscopy Database—SRD 20*, NIST Standard Reference Database 20, 2012.
(55) Grey, L. H.; Nie, H.-Y.; Biesinger, M. C. Defining the Nature of Adventitious Carbon and Improving Its Merit as a Charge Correction Reference for XPS. *Appl. Surf. Sci.* **2024**, *653*, No. 159319.
(56) Biesinger, M. C.; Payne, B. P.; Grosvenor, A. P.; Lau, L. W. M.; Gerson, A. R.; Smart, R. S. C. Resolving Surface Chemical States in XPS Analysis of First Row Transition Metals, Oxides and Hydroxides: Cr, Mn, Fe, Co and Ni. *Appl. Surf. Sci.* **2011**, *257* (7), 2717−2730.
(57) Sotoodeh, K. Carbon Dioxide (CO2) Corrosion. In *Case Studies of Material Corrosion Prevention for Oil and Gas Valves*; Sotoodeh, K., Ed.; Gulf Professional Publishing, 2022; pp 175−189. DOI: 10.1016/B978-0-323-95474-7.00007-X.
(58) Carlson, T. A.; McGuire, G. E. Study of the X-Ray Photoelectron Spectrum of Tungsten−Tungsten Oxide as a Function of Thickness of the Surface Oxide Layer. *J. Electron Spectrosc. Relat. Phenom.* **1972**, *1* (2), 161−168.
(59) Strohmeier, B. R. An ESCA Method for Determining the Oxide Thickness on Aluminum Alloys. *Surf. Interface Anal.* **1990**, *15* (1), 51−56.
(60) ASTM International. *Standard Practice for Exposure of Metals and Alloys by Alternate Immersion in Neutral 3.5% Sodium Chloride Solution*; ASTM International: USA, 2013.
(61) Frisch, M. J.; Trucks, G. W.; Schlegel, H. B.; Scuseria, G. E.; Robb, M. A.; Cheeseman, J. R.; Scalmani, G.; Barone, V.; Petersson, G. A.; Nakatsuji, H.; Li, X.; Caricato, M.; Marenich, A. V.; Bloino, J.; Janesko, B. G.; Gomperts, R.; Mennucci, B.; Hratchian, H. P.; Ortiz, J. V.; Izmaylov, A. F.; Sonnenberg, J. L.; Williams, F. Ding.; Lipparini, F.; Egidi, F.; Goings, J.; Peng, B.; Petrone, A.; Henderson, T.; Ranasinghe, D.; Zakrzewski, V. G.; Gao, J.; Rega, N.; Zheng, G.; Liang, W.; Hada, M.; Ehara, M.; Toyota, K.; Fukuda, R.; Hasegawa, J.; Ishida, M.; Nakajima, T.; Honda, Y.; Kitao, O.; Nakai, H.; Vreven, T.; Throssell, K.; Montgomery, J. A., Jr.; Peralta, J. E.; Ogliaro, F.; Bearpark, M. J.; Heyd, J. J.; Brothers, E. N.; Kudin, K. N.; Staroverov, V. N.; Keith, T. A.; Kobayashi, R.; Normand, J.; Raghavachari, K.; Rendell, A. P.; Burant, J. C.; Iyengar, S. S.; Tomasi, J.; Cossi, M.; Millam, J. M.; Klene, M.; Adamo, C.; Cammi, R.; Ochterski, J. W.; Martin, R. L.; Morokuma, K.; Farkas, O.; Foresman, J. B.; Fox, D. J.; et al. *Gaussian 09*; Gaussian Inc.: Wallingford, CT, 2016.
(62) Becke, A. D. Density-Functional Exchange-Energy Approximation with Correct Asymptotic Behavior. *Phys. Rev. A* **1988**, *38* (6), 3098−3100.
(63) Lee, C.; Yang, W.; Parr, R. G. Development of the Colle-Salvetti Correlation-Energy Formula into a Functional of the Electron Density. *Phys. Rev. B* **1988**, *37* (2), 785−789.
(64) Marenich, A. V.; Cramer, C. J.; Truhlar, D. G. Universal Solvation Model Based on Solute Electron Density and on a Continuum Model of the Solvent Defined by the Bulk Dielectric Constant and Atomic Surface Tensions. *J. Phys. Chem. B* **2009**, *113* (18), 6378−6396.
(65) Dennington, R.; Keith, T. A.; Millam, J. M. *GaussView*, version 6.1; Semichem Inc., 2016.
(66) Otsu, N. A Threshold Selection Method from Gray-Level Histograms. *IEEE Trans. Syst. Man Cybern.* **1979**, *9* (1), 62−66.
(67) Adsetts, J. R. Jadsetts/Pit Density Image Processing Calculator, 2024. https://github.com/jadsetts/PitDensityImageProcessingCalculator.

https://doi.org/10.1021/acs.chemmater.4c01804
Chem. Mater. 2025, 37, 76−86